A long-term (2005-2016) dataset of hourly integrated land-atmosphere interaction observations on the Tibetan Plateau

Yaoming Ma[1,3,4], Zeyong Hu[2,3], Zhipeng Xie[1,2], Weiqiang Ma[1,3], Binbin Wang[1], Xuelong Chen[1], Maoshan Li[5], Lei Zhong[6,7], Fanglin Sun[2], Lianglei Gu[2], Cunbo Han[1], Lang Zhang[1], Xin Liu[1], Zhangwei Ding[1], Genhou Sun[8], Shujin Wang[2], Yongjie Wang[1], Zhongyan Wang[1]

[1] Key Laboratory of Tibetan Environment Changes and Land Surface Processes, Institute of Tibetan Plateau Research, Chinese Academy of Sciences, Beijing, 100101, China.
[2] Key Laboratory of Land Surface Process and Climate Change in Cold and Arid Regions, Northwest Institute of Eco-Environment and Resources, Chinese Academy of Sciences, Lanzhou, 730000, China.
[3] CAS Center for Excellence in Tibetan Plateau Earth Sciences, Beijing, 100101, China.
[4] University of Chinese Academy of Sciences, 100049, Beijing, China.
[5] School of Atmospheric Sciences, Chengdu University of Information Technology, Chengdu, 610025, China.
[6] School of Earth and Space Sciences, University of Science and Technology of China, Hefei, 230026, China.
[7] CAS Center for Excellence in Comparative Planetology, USTC, Hefei, 230026, China.
[8] School of Atmospheric Sciences, Sun Yat-sen University, Guangzhou, 510275, China.

Correspondence to: Yaoming Ma (ymma@itpcas.ac.cn), Zhipeng Xie (zp_xie@itpcas.ac.cn) and Binbin Wang (wangbinbin@itpcas.ac.cn)

Abstract. The Tibetan Plateau (TP) plays a critical role in influencing regional and global climate, via both thermal and dynamical mechanisms. Meanwhile, as the largest high-elevation part of the cryosphere outside the polar regions, with vast areas of mountain glaciers, permafrost and seasonally frozen ground, the TP is characterized as an area sensitive to global climate change. However, meteorological stations are sparsely and biased distributed over the TP, owing to the harsh environmental conditions, high elevations, complex topography, and heterogeneous surfaces. Moreover, due to the weak representation of the stations, atmospheric conditions and the local land-atmosphere coupled system over the TP as well as its effects on surrounding regions are poorly quantified. This paper presents a long-term (2005-2016) in-situ observational dataset of hourly land-atmosphere interaction observations from an integrated high-elevation and cold region observation network, composed of six field stations on the TP. These in-situ observations contain both meteorological and micrometeorological measurements including gradient meteorology, surface radiation, eddy covariance (EC), soil temperature and soil water content profiles. Meteorological data were monitored by automatic weather stations (AWS) or planetary boundary layer (PBL) observation systems. Multilayer soil temperature and moisture were recorded to capture vertical hydrothermal variations and the soil freeze-thaw process. In addition, an EC system consisting of an ultrasonic anemometer and an infrared gas analyzer was installed at each station to capture the high-frequency vertical exchanges of energy, momentum, water vapor and carbon dioxide within the atmospheric boundary layer. The release of these continuous and long-term datasets with hourly resolution represents a leap forward in scientific data sharing across the TP, and it has been partially used in the past to assist in understanding key land surface processes. This dataset is described here comprehensively for facilitating a broader multidisciplinary community by enabling the evaluation and development of existing or new remote sensing algorithms as

well as geophysical models for climate research and forecasting. The whole datasets are freely available at Science Data Bank (http://www.dx.doi.org/10.11922/sciencedb.00103, Ma et al., 2020) and, additionally at the National Tibetan Plateau Data Center (https://data.tpdc.ac.cn/en/data/b9ab35b2-81fb-4330-925f-4d9860ac47c3/).

1 Introduction

The Tibetan Plateau (TP) is the world's highest and largest plateau with highly complex terrain and is referred as the "Third Pole of the World" (Qiu,2008). Moreover, the TP has the most extensive high-elevation distribution of cryosphere outside the polar regions. There are vast areas of mountain glaciers, snow, permafrost and seasonally frozen earth across the TP (Zhou and Guo, 1982;Kang et al., 2010;Cheng and Jin, 2013). Therefore, it also acts as the "Water Tower of Asia" (Immerzeel et al., 2010). Numerous researches indicate that the TP plays an essential role in controlling regional and global climate through its thermal and mechanical mechanisms (Manabe and Broccoli, 1990;Yanai et al., 1992;Duan and Wu, 2005;Liu et al., 2007). It exerts a major control on atmospheric circulation at the local and continental scale (Ding, 1992;Ye and Wu, 1998;Li et al., 2018) through its latent heat release (Wu et al., 2016) and interactions between the Asian monsoon and mid-latitude westerlies (Yao et al., 2012). Meanwhile, the TP is highly sensitive to climate change (Pepin and Lundquist, 2008;Kang et al., 2010;Chen et al., 2015). It is the driving force for regional environmental changes, and it amplifies environmental changes to global scale as well (Pan et al., 1996;Kang et al., 2010).

Land-atmosphere interactions over the TP play a crucial role in controlling the hemispheric atmospheric circulation pattern and climate evolution (Yang et al., 2004;Duan and Wu, 2005;Xiao and Duan, 2016;Li et al., 2018). Previous studies have revealed that accurate simulation of water and heat flux exchanges between the land surface and the atmosphere is a pivotal step towards improving the predictability and the projection accuracy of the climate system (Sellers et al., 1997;Pitman, 2003); this can be achieved through a comprehensive and accurate understanding of the land-atmosphere interactions based on in-situ observations (Yang et al., 2009). However, compared with other terrestrial regions of the world, observational data are scarce over the TP, owing to its vast geographic area with steep terrain, varied landforms, complex and diverse climates, harsh environmental conditions. The sparse and biased spatial distribution of observation stations is hard to match the high degree of landscape heterogeneity over the TP. In addition, high uncertainties in the satellite-retrieved land and atmospheric environmental variables of the TP impair the establishment of continuous, long-term regional-scale observations in remote areas of the TP. The lack of sufficient observational data limits our understanding of the interactions between the different earth spheres with heterogeneous land surface conditions and hinders the development of parameterization schemes in some critical physical processes of the land surface and atmospheric boundary layer, thereby, leading to associated uncertainties in estimating the past, present, and future climate change and its impacts. Therefore, it is essential to improve the atmospheric observation capability on the TP and its surrounding areas and obtain accurate atmospheric physical parameters for the near-surface and boundary layers over the TP, which can significantly contribute to the scientific understanding of the weather, climate and environmental changes, as well as their impacts, from regional scale (TP) to global scale.

To mitigate the scarcity of observational data and to improve our understanding of the coupled local land-atmosphere system and its effects, a series of atmospheric field experiments have been carried out over the TP since the 1970s. For example, the first Qinghai-Xizang Plateau Meteorology Experiment (QXPMEX) (Tao et al., 1986), the Global Energy and Water Cycle Experiment (GEWEX) Asian Monsoon Experiment (GAME)/Tibet intensive observation (Wang, 1999), the Coordinated Enhanced Observing Period (CEOP) Asia–Australia Monsoon Project on the Tibetan Plateau (CAMP/ Tibet) (Ma et al., 2006), and so on. Based on these meteorological experiments, several field observational stations have been established and kept on operation as yet. After decades of effort, with an optimized scientific design and layout, the synthesis level of atmospheric observation has been greatly enhanced and improved with respect to the observation infrastructure and technology used, and meteorological elements observed. With the construction of the Tibetan Observation and Research Platform (TORP, Ma et al., 2008) and the implementation of long-term multi-site collaborative field experiments, the limitations of the layout and function of the observation network over the TP have been mitigated to some extent. A large volume of land surface processes and PBL observations have been collected, and have played a crucial role in many disciplines, these including: land-atmosphere interactions (Wang et al., 2017;Xie et al., 2018;Zhong et al., 2019), the characteristics of the PBL and troposphere (Sun et al., 2006;Li et al., 2012;Ma et al., 2015;Chen et al., 2016), and the development of land surface parameterization schemes (Yang et al., 2003;Chen et al., 2013).

The aforementioned field experiments and multi-site collaborative observations have yielded significant progress in advancing our understanding of the land-atmosphere interactions. However, integrated observations from field stations over the TP are still not open for sharing and only very limited data are accessible. For instance, some in-situ observations can be obtained only through cooperation; others are restricted (e.g., only limited variables during a specified period are provided). Although some meteorological data can be requested from the National Tibetan Plateau Data Center (TPDC) in recent years (http://www.tpdc.ac.cn), only the daily mean values are provided, which are commonly lack of consistent and information of standard data processing methods. Furthermore, the temporal resolution of these daily mean value is too coarse for the land surface and climate modeling community, for which at least hourly values are required to run models and to evaluate detailed physical models. To overcome the above issues, a continuous and long-term integrated observational dataset of land-atmosphere interaction with high temporal resolution is now provided (Ma et al., 2020). The underlying observation network is composed of six stations over the TP. At each station, the following measurements are available: meteorological gradient, surface radiation, EC and soil hydrothermal. This dataset is released in a unified format that can be easily accessed and used by many communities, aiming to facilitate the consistency and continuity in scientific understanding of the interactions among the multi-sphere coupled systems over the TP. We expect this dataset will be widely used in studying the environment of the "Third Pole", especially by the atmosphere, hydrology, ecology and cryosphere communities. We also hope this dataset will promote the sharing, opening and value-added exploitation of the in-situ land-atmosphere interaction observations over the TP.

In this paper, we introduce and provide access to the long-term hourly dataset of the integrated land-atmosphere interaction observations over the TP. The integrated land-atmosphere interaction observation network is first described in Section 2. Section 3 deals specifically with a description of the meteorological, solar radiation, EC and soil hydrothermal data,

and presents an overview of the observation infrastructure, highlighting differences and similarities between the stations with respect to the observation items, and their variations at diurnal, daily and monthly scales. The availability of this dataset is documented in Section 4 and a final summary is presented in Section 5.

2 Site descriptions

The integrated land-atmosphere interaction observation network in this study consists of six field stations (Figure 1): the Muztagh Ata Westerly Observation and Research Station, Chinese Academy of Sciences (MAWORS, CAS); the Ngari Desert Observation and Research Station, CAS (NADORS); the BJ site of Nagqu Station of Plateau Climate and Environment, CAS (NPCE-BJ, hereinafter abbreviated to BJ) in the central TP; the Nam Co Monitoring and Research Station for Multisphere Interactions, CAS (NAMORS), as well as the Qomolangma Atmospheric and Environmental Observation and Research Station, CAS (QOMS) in the north region of Mt. Everest; and the Southeast Tibet Observation and Research Station for the Alpine Environment, CAS (SETORS).

The MAWORS station was located in the region where the atmospheric circulation was influenced by the westerly wind all year round. Soil at this station was predominately sandy soil and gravel with sparse and short grass-covered. Large scale modern glaciers are distributed around the station (the standard deviation of elevation within a kilometer around the station is 152.92 m, which is the highest among the six stations as shown in Table 1) and exert great influence on the local weather and climate. The observations from this station are of great significance for the study of interactions between westerly winds and monsoon and their effects on land-glacier-atmosphere changes, as well as changes in snow and ice resources.

The NADORS station was built in a flat and open mountain valley in the northwestern TP (with the lowest standard deviation of elevation). The land use type here is Gobi Desert with very short grasses (about 1-2 cm) on the sandy soil and gravel surface. It is located at the convergence zone of the Indian monsoon and westerly wind, where these two atmospheric circulations interact intensively, making the NADORS as an excellent location for the study of westerly-monsoon interactions on the desert landscape.

The BJ site is located in a flat, open prairie except for the north, where there stand low hills (the standard deviation of elevation is 15.14 m). The site is well-vegetation-covered and the dense grasses are relatively high with height up to 5 cm. Soil at the site is predominantly sandy silt loam. The BJ site is an ideal place to observe the land-atmospheric interactions on the alpine meadow ecosystem.

The NAMORS station is located on the banks of Lake Nam Co, with the Nyainqentanglha Mountain behind. The land is covered by alpine meadows and the soil type is predominantly sandy silt loam, but the gravel content is high at 30-40 cm below the ground. As lake has a significant influence on the atmospheric circulation in this region, and plays a certain role in regulating temperature variation and precipitation, etc. Thus, this station is an ideal place to measure the land-atmosphere interactions in the water-land-mountain mesoscale system.

The QOMS is situated at the bottom of the lower Rongbuk Valley, to the north of Mt. Everest. The surface is barren and the ground is relatively flat and open, with sparse and short vegetation. Sand and gravel dominant here from surface to deep soil. The Himalayas acts as the channel for the exchange of energy and materials between surface and tropospheric atmosphere. Moreover, local circulation patterns, such as valley winds, link the near-surface atmosphere on the north side of Mt. Everest with the upper free atmosphere, making this region the best location for monitoring atmospheric conditions in the Northern Hemisphere.

The SETORS station lies in a mountain valley close to the forested southeastern TP (the terrain is highly heterogeneous, but is not as complex as the MAWORS). It's surrounded by a dense vegetation cover (mainly temperate needle-leaf trees and alpine meadows). The shallow soil here is well developed and the water-holding capacity of the soil is greatly enhanced due to the presence of organic matter, while the deep soil is predominantly gravel. The observations from the SETORS station are important for studying the water and heat transport along the alpine valleys by the South Asian monsoon, the alpine forest-glacier-atmosphere interactions, and the transport of hydrothermal components of the vertical belt in the mountainous regions.

This high-cold region observation network is an essential component of the meteorological observation platform over the TP, carrying out land surface processes observations in areas that are typical in geography while currently lack of in-situ observations. This network serves as key locations for field observations and experiments: in particular, for monitoring the interactions between geological processes and climate; for collecting first-hand, high-resolution records of modern environmental variations; and for monitoring land surface processes and atmospheric processes. The observation system at each station primarily includes the following four categories of measurements: meteorological variables either from the PBL tower or the AWS, solar radiation components, eddy covariance fluxes and soil hydrothermal conditions. The meteorological instruments consist of up to 5 levels of wind speed and direction, air temperature, relative humidity instruments, surface air pressure, and precipitation. The surface radiation components include the incoming and outgoing shortwave and longwave radiations. The open-path EC turbulent flux measurement system is used to sample the high frequency vertical turbulent fluxes of the sensible heat flux, latent heat flux and carbon dioxide flux. Vertical profiles of soil temperature and soil moisture content are measured by multilayer temperature probes and water content reflectometers (5 or 6 layers). A list of the observation items and instruments in detail can be found in Table 2. To ensure the accuracy and reliability of the observations, periodic inspection, maintenance and calibration are carried out by professional engineers. Meanwhile, all stations are manned except for the cold winter season, and the instruments are checked and data are collected and processed regularly.

3 Integrated land-atmosphere interaction observations

3.1 Meteorological observations

To fully characterize the meteorological conditions and their vertical distributions in the surface layer, instruments were installed at several heights on a multi-layer PBL tower (QOMS, NAMORS, SETORS and BJ). For stations without the PBL tower, meteorological variables are recorded by a one-layer AWS at MAWORS and two-layer AWS at NADORS. The layer

arrangements of sensors are not the same at these 6 stations. For example, five layers of wind speed and wind direction anemometers, air temperature and humidity probes were installed at QOMS and NAMORS; four layers of sensors were installed at SETORS; for BJ, three layers of wind and two layers of air temperature and relative humidity probes were available during 2006-2014, while four levels of these measurements were provided during 2015-2016 (see Table 2 for details). Besides, a surface pressure barometer and precipitation gauge are available at all the stations except MAWORS, where precipitation is not measured. The meteorological elements of each station are detailed in the following sections, starting with the observation infrastructure, and followed by variations of the climatological average meteorological variables (except for wind direction and precipitation) at the lowest level of each station. We should note that the term "climatological" here does not strictly follow the definition recommended by the World Meteorological Organization (WMO), for which averages are based on 30 years of data. Here, "climatological" refers to the period for which variables are available at each station. At BJ, the climatological averages of wind speed, air temperature, relative humidity and pressure were calculated from 2006 to 2014.

3.1.1 Wind speed and wind direction

Wind speed and wind direction were monitored using non-heated anemometers at NADORS, MAWORS, NAMORS, QOMS, and SETORS, while using heated ultrasonic anemometers at BJ. At NADORS and MAWORS, the horizontal wind variations were monitored at heights of 1.5 and 2 m above the ground, respectively. At the NAMORS and QOMS, wind speed was measured at heights of 1.5, 2, 4, 10 and 20 m, while wind direction was only available at 1.5, 10 and 20 m. At SETORS, wind speed and wind direction were measured at four levels (1.3, 4.94, 9.95 and 18 m). At BJ, three layers of wind speed (at heights of 0.91, 5.02 and 10.36 m) and one-layer wind direction (at a height of 10.36 m) were available from 2006 to 2014 while the wind speed and wind direction were available at four levels (1.5, 3, 6, and 12 m) during 2015-2016.

The climatological averaged wind speeds at diurnal, daily and monthly scales are shown in Figure 2 (a-c). Clear inner diurnal variations were observed, characterizing with a maximum in the afternoon and a constant wind speed in the early morning and throughout the night. At the diurnal scale, wind speed at SETORS showed the lowest diurnal variation throughout the year, while that at BJ showed the largest variations (the multi-year average here reached 8.13 m/s in the afternoon in January). At BJ, MAWORS, NADORS and NAMORS, the variations in wind speed in winter (December, January and February) were larger than those in the other seasons, while the greatest variability was observed in spring and early summer at QOMS. Significant differences exist in the climatological averaged monthly wind speeds at all stations, except at SETORS, where the wind speed ranged only from 0.79 to 1.26 m/s. Generally, the wind speed was relatively lower during the monsoon season than the non-monsoon periods, particularly at QOMS, BJ, NAMORS and MAWORS, where wind speeds in winter were the highest throughout the year, while the largest values of wind speed were observed in spring at NADORS.

3.1.2 Air temperature

Air temperature is available at different heights at NAMORS (1.5, 2.0, 4.0, 10 and 20 m), QOMS (1.5, 2.0, 4.0, 10 and 20 m), SETORS (1.3, 4.94, 9.95 and 18 m) and MAWORS (1.9 m). Air temperatures were recorded at a single height of 1.5

m at NDORS and two heights of 1.03 and 8.41 m at BJ during 2006 to 2014. Identical to the wind sensors configuration, an air temperature gradient observation system with temperature probes at four heights (1.5, 3.0, 6.0 and 12 m) was used at BJ since 2015.

The multi-year monthly averaged diurnal variations of air temperature (Figure 2d) show that the values at NAMORS, QOMS and MAWORS were below 0°C in November, December, January and February. At BJ, the air temperature in January were below 0°C and the maximum values in December and February were also around freezing temperature (1.17°C and 0.72°C, respectively). As shown in Figure 2e, the minimum daily air temperatures at BJ, MAWORS, NAMORS and NADORS dropped below 0°C from mid-October until the end of March or early April of the following year, but they were approximately 5°C higher at QOMS and SETORS. These differences in the variations in daily mean air temperature among stations are clearly shown in Figure 2f. In summer (June, July and August), the average daily and monthly air temperature at the lowest level at NADORS was the highest among the six stations. Moreover, a wide variability was detected in the multi-year daily mean air temperatures at SETORS, especially in late March to early April, late May, and early December (Figure 2e). This abnormal variation indicates an instrument failure in the air temperature observations at 1.3 m at SETORS. Although this issue has been detected, the air temperature data provided at present are in raw format without any post-processing applied. Consequently, careful inspection is crucial when air temperature observations are required. In subsequent work, stricter data quality controls will be applied to detect problematic data and quality flags will be provided for each observational element.

3.1.3 Humidity

The heights of the humidity sensors are the same as those of the air temperature probes. Besides the relative humidity, up to four layers of water vapor pressure observations are also available at MAWORS (1.9 m), NADORS (1.5 and 2.8 m) and BJ (only available for the period 2015-2016, at 1.5, 3, 6, and 12 m); the heights of the water vapor pressure sensors at BJ are consistent with the heights of air temperature during the period from 2015 to 2016. Note that the unit of water vapor pressure is kPa at MAWORS and NADORS, while it is 0.1 hPa at BJ.

The relative humidity showed obvious diurnal variations, peaking in the afternoon (Figure 2g). Compared with the magnitude of diurnal variations in summer, the diurnal range of relative humidity at SETORS in winter and spring was much greater, reaching 50%, and the maximum value of the average diurnal cycle of relative humidity was about 80%, which was also significantly higher than those at other stations. In contrast, the diurnal variability during the monsoon season was much smaller than that at BJ, QOMS, NAMORS and MAWORS. The monthly relative humidity was lowest at NADORS, however, there was a marked increase in summer due to the transition of mid-latitude westerlies to the Asian summer monsoon. Differences in humidity among the six stations presented in the diurnal and daily relative humidity records were clearly reflected in the seasonal variations at the monthly scale.

3.1.4 Air pressure

Barometers produced by Vaisala were installed at each station. Compared with variations in wind speed, air temperature and relative humidity, the diurnal and seasonal variations in air pressure were not obvious (Figure 2j-l), and pressure remained at a relatively stable level throughout the year. Air pressure is elevation-dependent amongst the six stations, with the highest value at SETORS and the lowest value at NAMORS, while a consistent diurnal and seasonal variations were found both at QOMS and NADORS of similar altitude.

3.1.5 Precipitation

Precipitation is measured at all stations except for MAWORS, either with tipping buckets or weighting gauges. At BJ and NADORS, the cumulative precipitation is recorded, while the total half-hourly precipitation is recorded at NAMORS, QOMS and SETORS. For the cumulative precipitation, negative growth resulting from the evaporation from the rain gauge can seriously affect the measurement accuracy. Moreover, large errors can be introduced in the precipitation time series by wind-induced under-catch, wetting loss, evaporation loss, and underestimation of trace precipitation amounts; it is difficult to apply bias correction to account for these losses (Goodison et al., 1998). While precipitation data are extremely valuable, accurate measurement is notoriously difficult due to the large errors mentioned above, particularly in cold regions such as the TP. Therefore, in the released datasets, the precipitation data are provided in raw format without any post-processing, which might potentially be underestimated, thus further bias correction or data selection is necessary before the precipitation observations are used.

3.2 Surface radiations

Surface radiations are an important component of surface meteorological observations and are released as a separate category. A four-component radiation flux observing system was installed at each station. The surface radiation flux monitoring system consists of upward and downward pyranometers for outgoing and incoming shortwave radiation flux; and upward and downward pyranometers for outgoing and incoming long-wave radiation flux.

Figure 3a-c shows that the diurnal variations in downward shortwave radiation flux at QOMS were the highest among the six stations, and the largest amplitude occurred in April with a range of 0-1027W m^{-2}. In winter, the MAWARS showed the smallest diurnal variation in downward shortwave radiation flux, while the variations at SETORS were the smallest in other seasons. When combined with the relatively higher solar radiation flux in this area, variations in upward shortwave radiation flux at QOMS were relatively high (Figure 3d). The multi-year averaged daily series showed wide fluctuations in upward shortwave radiation at NAMORS in September and October, as well as at QOMS in the winter and spring (Figure 3e), which may result from high fractional snow cover during these periods. In the early stage of the summer monsoon, the downward shortwave radiation decreased gradually with increasing cloud cover, as a result of the increase of moisture in the upper atmosphere. Both the incoming and outgoing long-wave radiation flux at each station (Figure 3g-i and 3j-l, respectively)

showed significant seasonal variations, with high values in summer and low values in winter because of its dependence on air
260 and ground temperatures. Upward longwave radiation flux at QOMS was higher than that at other stations (excluding SETORS) except in July and August when NADORS showed the largest values (Figure 3k and 3l, note the time series of longwave radiation fluxes at SETORS are not plotted in Figure 3 because of monitoring problems, but some of the remaining valid observations show that the longwave radiation fluxes at SETORS are the largest among all the stations). These differences showed high consistency with the differences in uppermost layer soil temperature as shown in Figure 5d-f.

265 ## 3.3 EC data

The EC technique was applied to provide high-quality and continuous surface turbulent flux data for momentum, sensible, and latent heat. The EC system comprises a sonic anemometer (CSAT3, Campbell Scientific, Inc.) and a fast-response gas analyzer (LI-7500 open-path gas analyzer, Li-COR). All of the turbulence data were processed and quality-controlled using the TK3 software package (Mauder and Foken, 2011); the main processing procedures were as follows: excluding physically
270 invalid values and spikes, revising the time delay of the high-frequency water vapor and carbon dioxide sampling, planar fit coordinate rotation, correction of the loss of frequency response, correction of the ultrasonic virtual temperature and density fluctuations. The quality of each turbulent flux data series was evaluated by using the stationarity test and integral turbulence characteristics test. By combining the quality flags for stationarity and the integral turbulence characteristics test, a final quality flag (1-9) was assigned to each specific turbulent flux value except those for BJ, where classes 0-2 were used. Classes 1-3 (or
275 0 at BJ) indicate good quality suitable for fundamental research purposes, and classes 4-6 (1 at BJ) indicate suitability for general use, such as long-term analysis. Classes 7-9 (2 at BJ) should be discarded. The multi-year diurnal variation and seasonal variation of sensible and latent heat flux were calculated based on the data with medium or higher quality.

3.3.1 Sensible heat flux

As can be seen from the diurnal variations of sensible heat flux in Figure 4a, the sensible heat fluxes at all stations were
280 negative at night. During the period from March to October, the atmospheric heating effect on the ground at NADORS was the strongest during the night, while the magnitude of diurnal variation in the sensible heat flux was the lowest here among the six stations from April to September. The variations in sensible heat flux (Figure 4a-c) show that prior to the monsoon season, and the sensible heat flux was the main consumer of surface available energy, then the diurnal variation in sensible heat flux decreased significantly with the onset of summer monsoon and was comparable to the latent heat flux. In other words, sensible
285 heat flux exchanges prevail during the pre-monsoon periods. The timing of the onset of decreasing sensible heat flux following the spring maximum varied, occurring earliest at SETORS and NAMORS, followed by BJ and NADORS. Influenced by the interactions between the midlatitude westerlies and the summer monsoon, the summer sensible heat fluxes were significantly lower than those in spring at all stations.

3.3.2 Latent heat flux

290   In contrast to the bimodal pattern of the seasonal variations in sensible heat flux, the seasonal variation in latent heat flux revealed a unimodal pattern, that is, the latent heat flux was small during the pre-monsoon period, and when monsoon outbreaks, it increased rapidly as precipitation became frequent and the surface soil turned wet. The latent heat flux then increased gradually and it became comparable to the sensible heat flux during the summer monsoon period. A comparison of the seasonal variation of sensible heat flux (Figure 4c) and latent heat flux (Figure 4f) reveals that the latent heat flux was more significant

295   to the sensible heat flux during the Asia summer monsoon season. During this period, the latent heat flux predominated in the surface energy budget (excluding the QOMS and NADORS), and the magnitudes of diurnal variations of latent heat flux were greatest at SETORS and BJ, and weakest in the desert landscapes of QOMS and NADORS (Figure 4d).

3.3.3 Carbon dioxide flux

The carbon dioxide flux is an important component of the atmospheric carbon balance and is a very important variable in

300   the study of global climate change. As one of the key components of the EC monitoring system, the observed carbon dioxide fluxes at each station are provided through the density correction and frequency response correction applied by the TK3 software package (Mauder and Foken, 2011). A previous study has reported that the self-heating of the infrared gas analyzer in the open-path EC system can cause notable differences in temperature between the observation path and the ambient air, which may result in signal distortion (Burba et al., 2008); therefore, it is necessary to apply a specific correction to the carbon

305   dioxide flux data to eliminate the heating impact and to accurately reveal the intensity of carbon dioxide exchange in the TP ecosystem (Zhu et al., 2012). However, the heating effect of the instrument was not been considered in the carbon dioxide flux data provided in this manuscript, more detailed information can refer to the studies of Burba et al. (2008) and Zhu et al. (2012). When these data are used in studies of carbon dioxide exchange or related works (for example, estimating the net ecosystem production and its components), this specific correction of the data is needed to fully account for the impact of instrumental

310   heating on observations.

3.4 Soil hydrothermal observations

3.4.1 Ground surface temperature

Ground temperatures at NADORS, SETORS and BJ are provided in this dataset. The variations in ground temperature show the weakest diurnal variations at BJ and the strongest at SETORS, where the ground temperature during the night was

315   highest among the six stations. On the daily scale, the daily mean ground temperature at BJ was lower than that at SETORS and NADORS throughout the year, although its amplitude of the diurnal cycles was larger than that at the other two stations owing to the lower night-time temperatures (Figure 5a). Daily mean and monthly ground temperatures at BJ dropped below 0 °C during all months from October to April.

3.4.2 Soil temperature and soil moisture

320   Soil temperature and soil moisture are key physical quantities characterizing the land surface conditions and play important roles in controlling the energy and mass interactions between land and the overlying atmosphere. To capture the continuous, real-time soil thermal and soil moisture conditions on different ground surfaces of the TP, five layers of soil profile sensors (soil temperature probes and water content reflectometers) were installed at SETORS (4, 10, 20, 60 and 100 cm), MAWORS (10, 20, 40, 80 and 160 cm) and NADORS (0, 20, 50, 100 and 200 cm). At NAMORS and QOMS, soil temperature

325   and soil moisture were observed at depths of 0, 10, 20, 40, 80 and 160 cm. At BJ, soil temperature and soil water content were measured at four depths (0, 4, 10, 20 and 40 cm) during 2006-2014, and then at six depths (5, 10, 20, 40, 80 and 160 cm) during 2015-2016.

Figure 5a-f and Figure 5g-i demonstrate the variations of soil temperature and soil moisture, respectively, in the uppermost layer of each station (i.e., the top layer after excluding observations at a depth of 0 cm). Specifically, these were at depths of 4

330   cm at SETORS and BJ, 10 cm at MAWORS, NAMORS and QOMS, and 20 cm at NADORS. Soil temperature in the shallow layers show obvious variation at the diurnal scale, and are highly consistent with the variations in air temperature. The soil water content quickly responded to precipitation with an obvious increase with the onset of summer monsoon, particularly at BJ. Wiring problems at SETORS caused erroneous soil temperature and soil water content readings in all layers, which seriously affected the reliability of the respective observations. Although the two variables from SETORS are available in this

335   dataset, data quality control and correction are needed.

3.4.3 Soil heat flux

Soil heat flux was measured by soil heat flux plates buried at BJ (10 and 20 cm for 2006-2014, 5 and 10 cm for 2015-2016), QOMS (10 cm) and SETORS (4, 10, 20, 60 and 100 cm). All the available soil heat flux data at each depth are released through this data descriptor. Due to abnormal fluctuations of the top-layer soil heat flux at QOMS and SETORS at both the

340   diurnal and daily scale, only the variations in top-layer soil heat flux at BJ site were presented in Figure 5. The soil heat flux at BJ showed that it was usually relatively small and had evident diurnal and seasonal variations.

4 Data availability

Raw data were converted from binary mode to ASCII mode, and then key variables were extracted and saved as comma-separated values (.csv format). The CSV format was chosen as it is one of the most widely supported structured data format in

345   scientific applications. The plausible value check, time consistency check, and internal consistency check were applied to ensure the accuracy and reliability of the observations. However, to retain the observations in their original form as much as possible, there is no further process taken except for replacing outliers with missidng value (NaN). Data consistency check procedures were applied to ensure the accuracy and reliability of the observations, but the data quality flag is not available for the moment. Some time series of observations should be used with caution (for example, the soil hydrothermal data in

350 SETORS), as anomalous changes or values were detected. In this case, further procedures such as bias correction or data selection are required. The local time was used in all the data files (UTC+8). All datasets presented and described in this article have been released and are available to free download from the Science Data Bank (http://www.dx.doi.org/10.11922/sciencedb.00103, Ma et al., 2020) and the TPDC (https://data.tpdc.ac.cn/en/data/b9ab35b2-81fb-4330-925f-4d9860ac47c3/). Special compressed files were designated for each station with four categories: turbulent

355 flux data (FLUX), gradient meteorological data (GRAD), soil hydrothermal data (SOIL) and radiation data (RADM). Meanwhile, the data integrity of each variable was also provided every year, with a value of 100 representing the absence of missing data. The heat maps shown in the Supplement are used to provide the data integrity information. These maps are very useful as they provide an intuitive depiction of the availability of each variable, facilitating data selection when analyzing land-atmosphere interactions and the structure of the PBL, driving land surface models, or evaluating model results.

360 **5 Summary**

As in-situ observations are scarce yet invaluable in cold regions, the model parameterization schemes are generally developed and evaluated based on a small number of sites, of which very few are located in high mountainous regions. Current numerical models suffer from a poor representation of the cold region processes, particularly on the TP (Xia et al., 2014;Toure et al., 2016;Orsolini et al., 2019;Xie et al., 2019). Long-term, high-quality and high temporal resolution observational data in

365 the Third Pole region are not only extremely scarce, but are also very important for a deeper understanding of the key land surface processes. In this paper, a suite of land-atmosphere interactions observations from the integrated observation network over the TP is presented. Compared with previously open-accessed daily meteorological observations over the TP, this dataset provides the most comprehensive and high-quality continuous in-situ observations, with the highest temporal resolution (hourly) to date. Therefore, this fine-resolution data product can help to promote comprehensive scientific understanding of

370 the interactions among the multi-sphere coupled systems over the TP and even the globe; to quantify uncertainties in satellite and model products; to assess the biases and gaps existing between the model simulations and reality; and to facilitate the development and improvement of land surface process models in cold regions. We believe that the datasets presented in this paper will contribute to these research areas and that they will be widely used in model development and evaluation.

375 **Author contributions.** YMM, ZYH, ZPX and BBW led the writing of this article and endorse the responsibility of the experimental site and the instruments. YMM and ZPX drafted the manuscript and ZPX led the consolidation of the dataset, prepared the data in the standardized format described in this paper and wrote this manuscript together with all co-authors.

Competing interests. The authors declare that they have no conflict of interests.

380

Acknowledgments. We would like to thank all the scientists, engineers, and students who participated in the field observations, maintained the observation instruments, and processed the observations.

Financial support. This work was supported by the Second Tibetan Plateau Scientific Expedition and Research (STEP) program (2019QZKK0103), the Strategic Priority Research Program of Chinese Academy of Sciences (XDA20060101), the National Natural Science Foundation of China (91837208), the National Key Research and Development Program of China (2018YFC1505701) and the National Natural Science Foundation of China (41905012, 41835650, 41975009, 41875031, 91737205, 41675106).

References

[1]. Burba, G. G., McDERMITT, D. K., Grelle, A., Anderson, D. J., and Xu, L.: Addressing the influence of instrument surface heat exchange on the measurements of CO2 flux from open-path gas analyzers, Global Change Biology, 14, 1854-1876, 2008.

[2]. Chen, D., Xu, B., Yao, T., Guo, Z., Cui, P., Chen, F., Zhang, R., Zhang, X., Zhang, Y., Fan, J., Hou, Z., and Zhang, T.: Assessment of past, present and future environmental changes on the Tibetan Plateau, Chinese Science Bulletin, 60, 3025, https://doi.org/10.1360/N972014-01370, 2015.

[3]. Chen, X., Su, Z., Ma, Y., Yang, K., Wen, J., and Zhang, Y.: An Improvement of Roughness Height Parameterization of the Surface Energy Balance System (SEBS) over the Tibetan Plateau, Journal of Applied Meteorology and Climatology, 52, 607-622, 10.1175/jamc-d-12-056.1, 2013.

[4]. Chen, X., Škerlak, B., Rotach, M. W., Añel, J. A., Su, Z., Ma, Y., and Li, M.: Reasons for the Extremely High-Ranging Planetary Boundary Layer over the Western Tibetan Plateau in Winter, Journal of the Atmospheric Sciences, 73, 2021-2038, 10.1175/jas-d-15-0148.1, 2016.

[5]. Cheng, G., and Jin, H.: Permafrost and groundwater on the Qinghai-Tibet Plateau and in northeast China, Hydrogeology Journal, 21, 5-23, 10.1007/s10040-012-0927-2, 2013.

[6]. Ding, Y.: Effects of the Qinghai-Xizang (Tibetan) plateau on the circulation features over the plateau and its surrounding areas, Advances in Atmospheric Sciences, 9, 112-130, 10.1007/BF02656935, 1992.

[7]. Duan, A. M., and Wu, G. X.: Role of the Tibetan Plateau thermal forcing in the summer climate patterns over subtropical Asia, Climate Dynamics, 24, 793-807, 10.1007/s00382-004-0488-8, 2005.

[8]. Goodison, B. E., Louie, P. Y., and Yang, D.: WMO solid precipitation measurement intercomparison, World Meteorological Organization Geneva, Switzerland, 1998.

[9]. Immerzeel, W. W., van Beek, L. P. H., and Bierkens, M. F. P.: Climate Change Will Affect the Asian Water Towers, Science, 328, 1382-1385, 10.1126/science.1183188, 2010.

[10]. Kang, S., Xu, Y., You, Q., Flügel, W.-A., Pepin, N., and Yao, T.: Review of climate and cryospheric change in the Tibetan Plateau, Environmental Research Letters, 5, 015101, 10.1088/1748-9326/5/1/015101, 2010.

[11]. Li, M., Ma, Y., and Zhong, L.: The Turbulence Characteristics of the Atmospheric Surface Layer on the North Slope of Mt. Everest Region in the Spring of 2005, Journal of the Meteorological Society of Japan. Ser. II, 90C, 185-193, 10.2151/jmsj.2012-C13, 2012.

[12]. Li, W., Guo, W., Qiu, B., Xue, Y., Hsu, P.-C., and Wei, J.: Influence of Tibetan Plateau snow cover on East Asian atmospheric circulation at medium-range time scales, Nature Communications, 9, 4243, 10.1038/s41467-018-06762-5, 2018.

[13]. Liu, Y., Hoskins, B., and Blackburn, M.: Impact of Tibetan Orography and Heating on the Summer Flow over Asia, Journal of the Meteorological Society of Japan. Ser. II, 85B, 1-19, 10.2151/jmsj.85B.1, 2007.

[14]. Ma, Y., Yao, T., and Wang, J.: Experimental study of energy and water cycle in Tibetan plateau——The progress introduction on the study of GAME/Tibet and CAMP/Tibet, Plateau Meteorology, 25, 344-351, 2006.

[15]. Ma, Y., Zhu, Z., Amatya, P. M., Chen, X., Hu, Z., Zhang, L., Li, M., and Ma, W.: Atmospheric boundary layer characteristics and land−atmosphere energy transfer in the Third Pole area, Proc. IAHS, 368, 27-32, 10.5194/piahs-368-27-2015, 2015.

[16]. Manabe, S., and Broccoli, A. J.: Mountains and Arid Climates of Middle Latitudes, Science, 247, 192-195, 10.1126/science.247.4939.192, 1990.

[17]. Mauder, M., and Foken, T.: Documentation and instruction manual of the eddy-covariance software package TK3, 2011.

[18]. Orsolini, Y., Wegmann, M., Dutra, E., Liu, B., Balsamo, G., Yang, K., de Rosnay, P., Zhu, C., Wang, W., Senan, R., and Arduini, G.: Evaluation of snow depth and snow cover over the Tibetan Plateau in global reanalyses using in situ and satellite remote sensing observations, The Cryosphere, 13, 2221-2239, 10.5194/tc-13-2221-2019, 2019.

[19]. Pan, B., Li, J., and Chen, F.: Qinghai-Xizang Plateau—a driver and amplifier of the global climatic change J, Lanzhou University (Natural Science Edition), 32, 08-115, 1996.

[20]. Pepin, N. C., and Lundquist, J. D.: Temperature trends at high elevations: Patterns across the globe, Geophysical Research Letters, 35, 10.1029/2008gl034026, 2008.

[21]. Pitman, A. J.: The evolution of, and revolution in, land surface schemes designed for climate models, International Journal of Climatology, 23, 479-510, 10.1002/joc.893, 2003.

[22]. Ran Y., Li, X.: Multi-source integrated chinese land cover map(2000). National Tibetan Plateau Data Center, 2019. DOI:10.11888/Socioeco.tpdc.270467.

[23]. Sellers, P. J., Dickinson, R. E., Randall, D. A., Betts, A. K., Hall, F. G., Berry, J. A., Collatz, G. J., Denning, A. S., Mooney, H. A., Nobre, C. A., Sato, N., Field, C. B., and Henderson-Sellers, A.: Modeling the Exchanges of Energy, Water, and Carbon Between Continents and the Atmosphere, Science, 275, 502-509, 10.1126/science.275.5299.502, 1997.

[24]. Sun, F., Ma, Y., Ma, W., and Li, M.: One observational study on atmospheric boundary layer structure in Mt. Qomolangma region, Plateau Meteorology, 25, 1014-1019, 2006.

[25]. Tao, S., Luo, S., and Zhang, H.: The Qinghai-Xizang Plateau Meteorological Experiment (Qxpmex) May–August 1979, Proceedings of International Symposium on the Qinghai-Xizang Plateau and Mountain Meteorology, 1986, 3-13,

[26]. Toure, A. M., Rodell, M., Yang, Z.-L., Beaudoing, H., Kim, E., Zhang, Y., and Kwon, Y.: Evaluation of the Snow Simulations from the Community Land Model, Version 4 (CLM4), Journal of Hydrometeorology, 17, 153-170, 10.1175/jhm-d-14-0165.1, 2016.

[27]. Wang, B., Ma, Y., Ma, W., and Su, Z.: Physical controls on half-hourly, daily, and monthly turbulent flux and energy budget over a high-altitude small lake on the Tibetan Plateau, Journal of Geophysical Research: Atmospheres, 122, 2289-2303, 10.1002/2016jd026109, 2017.

[28]. Wang, J.: Land surface process experiments and interaction study in China-From HEIFE to IMGRASS and GAME-TIBET/TIPEX, Plateau Meteorology, 18, 280-294, 1999.

[29]. Wu, G., Zhuo, H., Wang, Z., and Liu, Y.: Two types of summertime heating over the Asian large-scale orography and excitation of potential-vorticity forcing I. Over Tibetan Plateau, Science China Earth Sciences, 59, 1996-2008, 10.1007/s11430-016-5328-2, 2016.

[30]. Xia, K., Wang, B., Li, L., Shen, S., Huang, W., Xu, S., Dong, L., and Liu, L.: Evaluation of snow depth and snow cover fraction simulated by two versions of the flexible global ocean-atmosphere-land system model, Advances in Atmospheric Sciences, 31, 407-420, 10.1007/s00376-013-3026-y, 2014.

[31]. Xiao, Z., and Duan, A.: Impacts of Tibetan Plateau Snow Cover on the Interannual Variability of the East Asian Summer Monsoon, Journal of Climate, 29, 8495-8514, 10.1175/jcli-d-16-0029.1, 2016.

[32]. Xie, Z., Hu, Z., Xie, Z., Jia, B., Sun, G., Du, Y., and Song, H.: Impact of the snow cover scheme on snow distribution and energy budget modeling over the Tibetan Plateau, Theoretical and Applied Climatology, 131, 951-965, 10.1007/s00704-016-2020-6, 2018.

[33]. Xie, Z., Hu, Z., Ma, Y., Sun, G., Gu, L., Liu, S., Wang, Y., Zheng, H., and Ma, W.: Modeling Blowing Snow Over the Tibetan Plateau With the Community Land Model: Method and Preliminary Evaluation, Journal of Geophysical Research: Atmospheres, 124, 9332-9355, 10.1029/2019jd030684, 2019.

[34]. Yanai, M., Li, C., and Song, Z.: Seasonal Heating of the Tibetan Plateau and Its Effects on the Evolution of the Asian Summer Monsoon, Journal of the Meteorological Society of Japan. Ser. II, 70, 319-351, 10.2151/jmsj1965.70.1B_319, 1992.

[35]. Yang, K., Koike, T., and Yang, D.: Surface Flux Parameterization in the Tibetan Plateau, Boundary-Layer Meteorology, 106, 245-262, 10.1023/A:1021152407334, 2003.

[36]. Yang, K., Koike, T., Fujii, H., Tamura, T., Xu, X., Bian, L., and Zhou, M.: The daytime evolution of the atmospheric boundary layer and convection over the Tibetan Plateau: observations and simulations, Journal of the Meteorological Society of Japan. Ser. II, 82, 1777-1792, 2004.

[37]. Yang, K., Chen, Y.-Y., and Qin, J.: Some practical notes on the land surface modeling in the Tibetan Plateau, Hydrology and Earth System Sciences, 13, 687-701, 2009.

[38]. Yao, T., Thompson, L., Yang, W., Yu, W., Gao, Y., Guo, X., Yang, X., Duan, K., Zhao, H., Xu, B., Pu, J., Lu, A., Xiang, Y., Kattel, D. B., and Joswiak, D.: Different glacier status with atmospheric circulations in Tibetan Plateau and surroundings, Nature Climate Change, 2, 663-667, 10.1038/nclimate1580, 2012.

[39]. Ye, D.-Z., and Wu, G.-X.: The role of the heat source of the Tibetan Plateau in the general circulation, Meteorology and Atmospheric Physics, 67, 181-198, 10.1007/BF01277509, 1998.

[40]. Zhong, L., Zou, M., Ma, Y., Huang, Z., Xu, K., Wang, X., Ge, N., and Cheng, M.: Estimation of Downwelling Shortwave and Longwave Radiation in the Tibetan Plateau Under All-Sky Conditions, Journal of Geophysical Research: Atmospheres, 124, 11086-11102, 10.1029/2019jd030763, 2019.

[41]. Zhou, Y., and Guo, D.: Principal characteristics of permafrost in China, Journal of Glaciology and Geocryology, 1, 1982.

[42]. Zhu, X.-j., Yu, G.-r., Wang, Q.-f., ZHANG, M., HAN, S.-j., ZHAO, X.-q., and YAN, J.-h.: Instrument heating correction effect on estimation of ecosystem carbon and water fluxes, Chinese Journal of Ecology, 31, 487-493, 2012.

Table 1. List of the geographic characteristics of the six sites.

Site	Latitude	longitude	Elevation (m)	Elevation range (m)[*]	Standard deviation of elevation (m)[*]	Land cover	Soil type
BJ	31.37ºN	91.90ºE	4509	4438-4547	15.14	Alpine meadow	Sandy silt loam
QOMS	28.36ºN	86.95ºE	4298	4207-4508	44.44	Alpine desert	Sand and gravel
SETORS	29.77ºN	94.73ºE	3327	3267-3760	78.72	Alpine meadow	Sandy clay loam
NADORS	33.39ºN	79.70ºE	4270	4211-4308	11.99	Alpine desert	Sand and gravel
MAWORS	38.76ºN	75.05ºE	3668	3626-4327	152.91	Alpine desert	Sand and gravel
NAMORS	30.77ºN	90.98ºE	4730	4697-4806	14.09	Alpine steppe	Sandy silt loam

Note: * elevation range and standard deviation of elevation are calculated within a kilometer around the station based on the 30 m resolution ASTER DEM data (source: https://asterweb.jpl.nasa.gov/gdem.asp)

Table 2. Overview of the sensors used at each station.

Site	Variables	Sensors models	Manufacturers	Period	Heights	Units
BJ	Air temperature	HMP45D	Vaisala	2006-2014	1.03 and 8.41 m	°C
		HMP155	Vaisala	2015-2016	1.5, 3, 6, and 12 m	
	Wind speed and direction	05103	RM Young	2006-2014	0.91, 5.02, and 10.36 m	m/s
		WindSonic	Gill	2015-2016	1.5, 3, 6, and 12 m	
	Humidity	HMP45D	Vaisala	2006-2014	1.03 and 8.41 m	%
		HMP155	Vaisala	2015-2016	1.5, 3, 6, and 12 m	
	Pressure	PTB220C	Vaisala	2006-2014	-	hPa
	Radiations	CM21 for shortwave radiation	Kipp & Zonen	2006-2016	-	W m^{-2}
		PIR for longwave radiation	Eppley	2006-2016	-	
	Precipitation	NOAH-II	ETI	2006-2014	-	mm
		T200B	Geonor	2015-2016	-	
	Soil temperature	TS-301	Okazaki	2006-2014	0.04, 0.1, 0.2, and 0.4 m	°C
		TR-219L	Tri-Tronics	2015-2016	0.05, 0,1, 0.2, 0.4, 0.8 and 1.6 m	
	Soil moisture	CS616-L	Campbell	2006-2014	0.04 and 0.2m	v/v %
		CS616-L	Campbell	2015-2016	0.05, 0,1, 0.2, 0.4, 0.8 and 1.6 m	
	Soil heat flux	HFP01	Hukseflux	2006-2014	0.1and 0.2 m	W m^{-2}
		HFP01	Hukseflux	2015-2016	0.05 and 0.1 m	
	EC	CSAT3	Campbell	2006-2016	3.02 m	
		LI-7500	Li-COR			
QOMS	Air temperature	HMP45C-GM	Vaisala	2005-2016	1.5, 2, 4, 10, and 20 m	°C
	Wind speed and direction	034B	MetOne	2005-2016	1.5, 2, 4, 10, and 20 m	m s^{-1}
	Humidity	HMP45C-GM	Vaisala	2005-2016	1.5, 2, 4, 10, and 20 m	%
	Pressure	PTB220A	Vaisala	2005-2016	-	hPa
	Radiations	CNR1	Kipp & Zonen	2005-2016	-	W m^{-2}
	Precipitation	RG13H	Vaisala	2005-2016	-	mm
	Soil temperature	Model 107	Campbell	2005-2016	0, 0.1, 0.2, 0.4, 0.8 and 1.6 m	°C
	Soil moisture	CS616	Campbell	2005-2016	0, 0.1, 0.2, 0.4, 0.8 and 1.6 m	v/v %
	Soil heat flux	HFP01	Hukseflux	2005-2016	0.05 m	W m^{-2}
	EC	CSAT3	Campbell	2007-2016	3.25 m	
		LI-7500	Li-COR			
SETORS	Air temperature	HMP45C-GM	Vaisala	2007-2016	1.3, 4.94, 9.95, and 18 m	°C
	Wind speed and direction	034B	MetOne	2007-2016	1.3, 4.94, 9.95, and 18 m	m s^{-1}
	Humidity	HMP45C-GM	Vaisala	2007-2016	1.3, 4.94, 9.95, and 18 m	%
	Pressure	PTB220A	Vaisala	2007-2016	-	hPa
	Radiations	CNR1	Kipp & Zonen	2007-2016	-	W m^{-2}
	Precipitation	RG13H	Vaisala	2007-2016	-	mm
	Soil temperature	Model 107	Campbell	2007-2016	0.04, 0.1, 0.2, 0.6 and 1 m	°C

	Soil moisture	CS616	Campbell	2007-2016	0.04, 0.1, 0.2, 0.6 and 1 m	v/v
	Soil heat flux	HFP01	Hukseflux	2007-2016	0.04, 0.1, 0.2, 0.6 and 1 m	W m^{-2}
	EC	CSAT3	Campbell	2007-2016	3.04 m	m s^{-1}
		LI-7500	Li-COR			
NADORS	Air temperature	HMP45C	Vaisala	2009-2016	1.5 m	℃
	Wind speed and direction	05013	RM Young	2009-2016	1.5 m	m s^{-1}
	Relative humidity	HMP45C	Campbell	2009-2016	1.5 and 2.8 m	%
	Water vapor pressure	Unknow	Unknow	2009-2016	1.5 and 2.8 m	kPa
	Pressure	PTB210	Vaisala	2009-2016	-	hPa
	Radiations	NR01	Kipp & Zonen	2009-2016	-	W m^{-2}
	Precipitation	T-200B	Geonor	2009-2016	-	mm
	Soil temperature	CSI 109	Campbell	2011-2016	0, 0.2, 0.5, 1.0 and 2.0 m	℃
	Soil moisture	CS616	Campbell	2011-2016	0, 0.2, 0.5, 1.0 and 2.0 m	v/v
	EC	CSAT3 and LI-7500	Campbell and Li-COR	2005-2016	2.75 m	
MAWORS	Air temperature	HMP155A	Vaisala	2010-2016	1.9 m	℃
	Wind speed and direction	05103-L	RM Young	2010-2016	2 m	m s^{-1}
	Relative humidity	HMP155A	Vaisala	2010-2016	1.9 m	%
	Water vapor pressure	Unknow	Unknow	2010-2016	1.9 m	kPa
	Pressure	PTB210	Vaisala	2010-2016	-	hPa
	Radiations	NR01	Kipp & Zonen	2010-2016	-	W m^{-2}
	Soil temperature	CSI 109	Campbell	2010-2016	0.1, 0.2, 0.4, 0.8 and 1.60 m	℃
	Soil moisture	CS616	Campbell	2010-2016	0.1, 0.2, 0.4, 0.8 and 1.60 m	v/v
	EC	CSAT3	Campbell	2010-2016	2.3m	
		LI-7500	Li-COR			
NAMORS	Air temperature	HMP45D	Vaisala	2005-2016	1.5, 2.0, 4.0, 10.0 and 20.0 m	℃
	Wind speed and direction	WAA151	Vaisala	2005-2016	1.5, 2.0, 4.0, 10.0 and 20.0 m	m s^{-1}
	Humidity	HMP45D	Vaisala	2005-2016	1.5, 2.0, 4.0, 10.0 and 20.0 m	%
	Pressure	PTB210	Vaisala	2005-2016	-	hPa
	Radiations	CMP6	Vaisala	2005-2016	-	W m^{-2}
	Precipitation	RG13H	Vaisala	2005-2016	-	mm
	Soil temperature	Model 107	Campbell	2005-2016	0, 0.1, 0.2, 0.4, 0.8, 1.6 m	℃
	Soil moisture	CS616	Campbell	2005-2016	0, 0.1, 0.2, 0.4, 0.8, 1.6 m	v/v %
	EC	CSAT3	Campbell	2005-2016	3.06m	
		LI-7500	Li-COR			
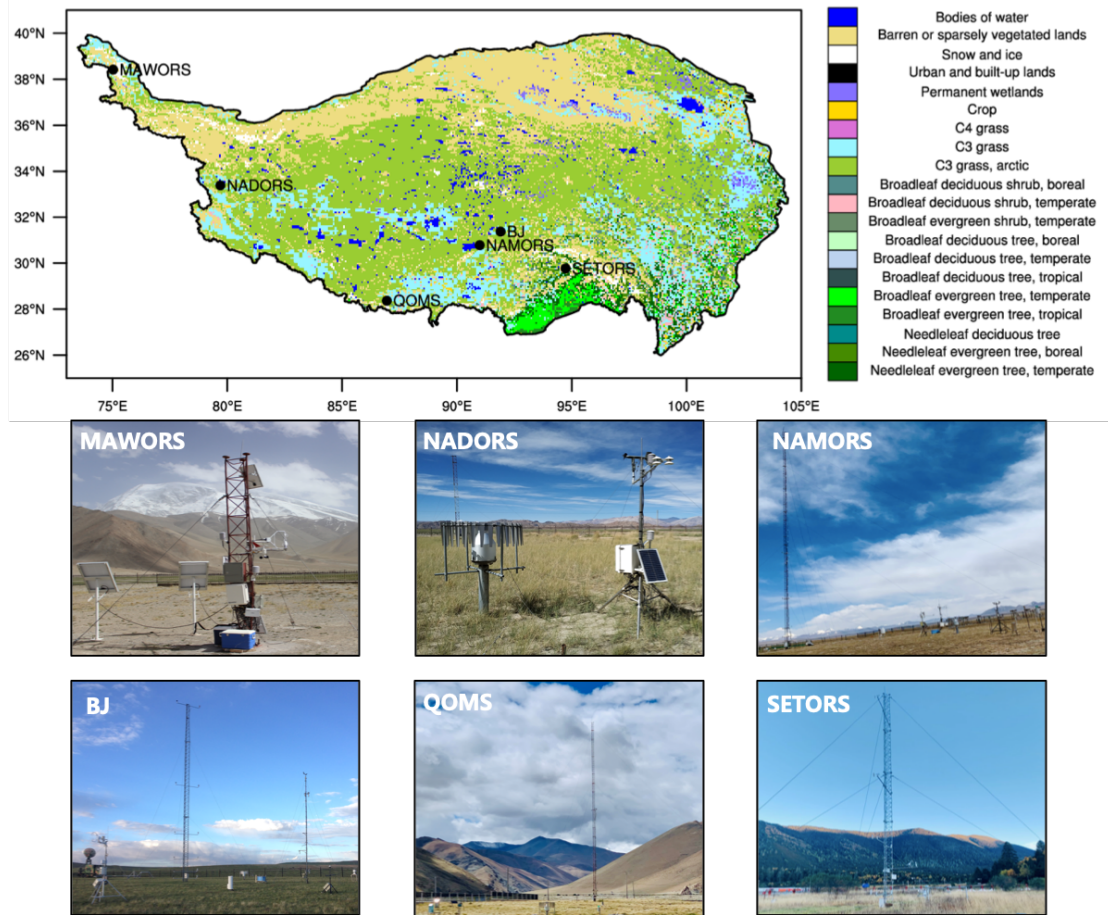
Figure 1. The integrated land-atmosphere observation network on the TP. At each site, the near surface atmospheric conditions are sampled with multilayer wind speed and direction, air temperature and humidity instruments. Surface pressure, precipitation and four-component surface radiation fluxes are also measured. Vertical profiles of soil temperature and soil moisture content are monitored by multilayer temperature probes and water content reflectometers. An open path eddy covariance turbulent measurement system is installed at each site to provide continuous monitoring of the vertical turbulent fluxes within the atmospheric boundary layers (The data source of the land cover map in the top of this figure is Ran and Li, 2019).
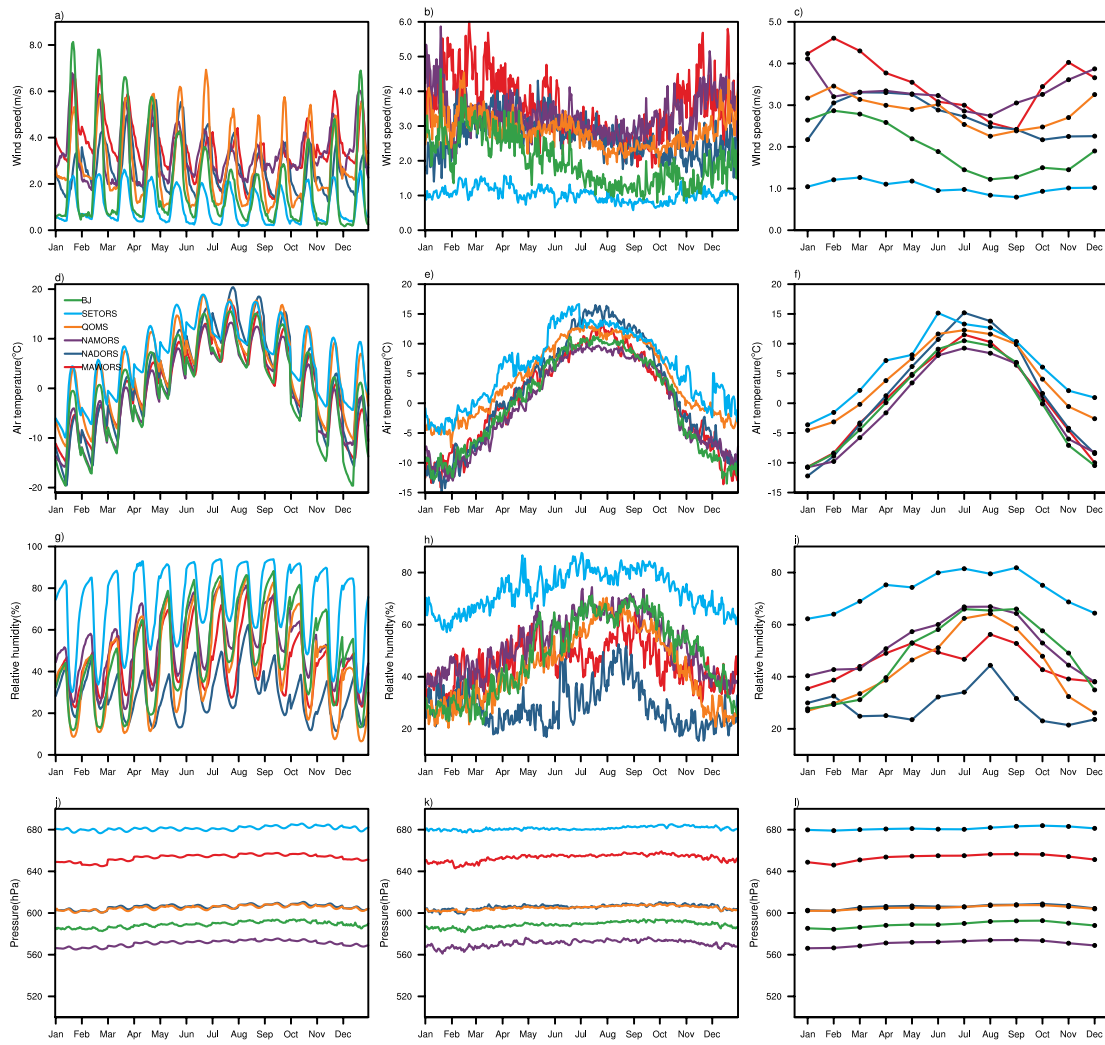
Figure 2. The climatological averages of the lowest-level of wind speed, air temperature, relative humidity and surface pressure at diurnal (left-most), daily (middle) and monthly (right-most) scales. For sites except BJ, the climatological mean of each variable was calculated based on all the available observations; for BJ, only the observations during the period of 2006-2014 were used. [Color figure can be viewed in the online issue].
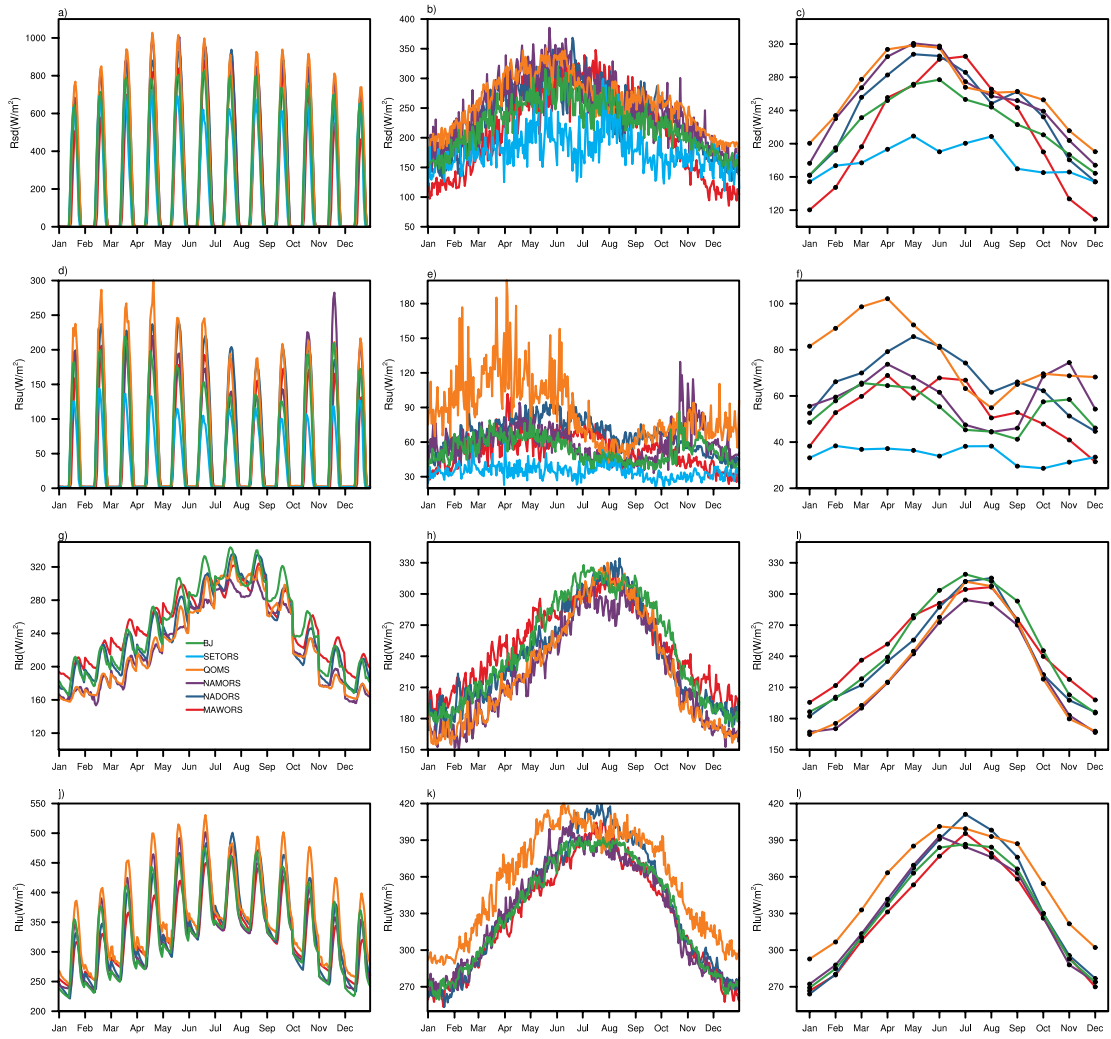
Figure 3. Same as Figure 2, but for the climatological average of the downward and upward solar radiation (Rsd and Rsu), and incoming and outgoing longwave radiation (Rld and Rlu), respectively. [Color figure can be viewed in the online issue].
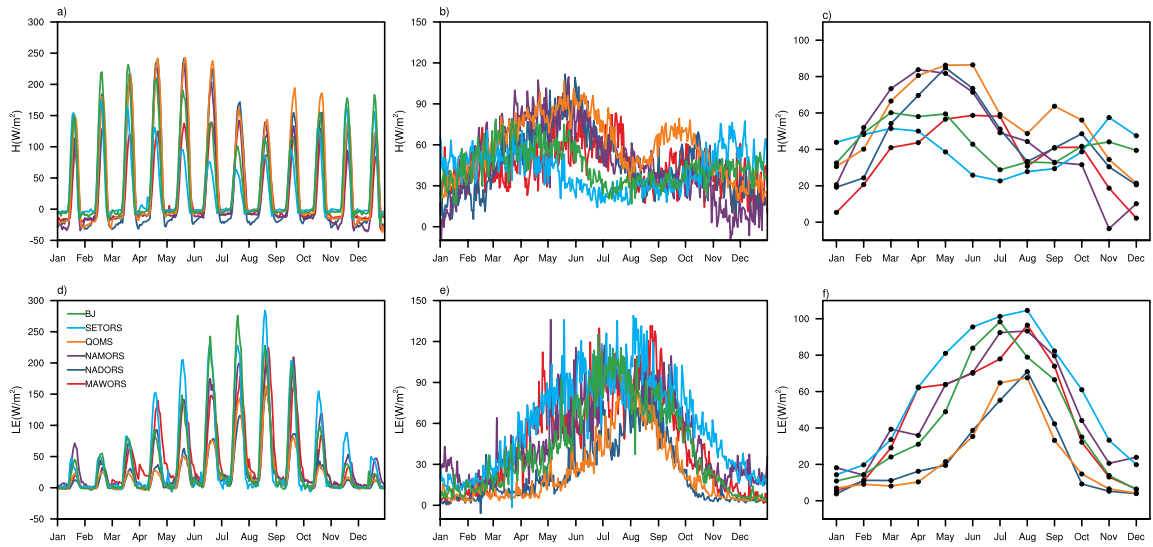
Figure 4. Same as Figure 2, but for the climatological average of the sensible heat flux (H) and latent heat flux (LE) variation, respectively. [Color figure can be viewed in the online issue].
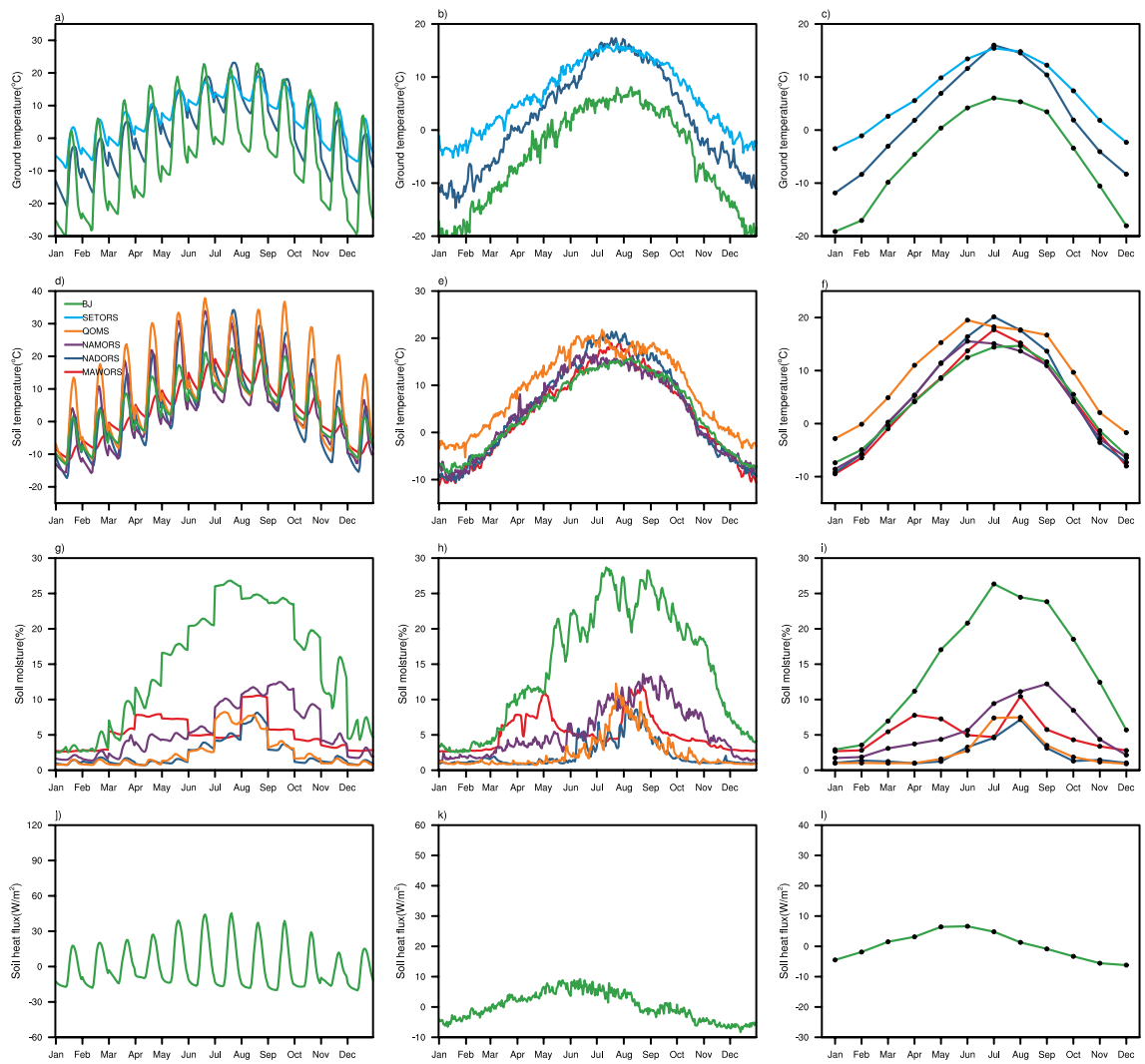
Figure 5. Same as Figure 2, but for the climatological average of ground temperature and first layer (except for the observations at depths of 0cm) soil temperature, soil moisture and soil heat flux, respectively. [Color figure can be viewed in the online issue].